




Concept of Modal Repulsion for Examining the Subsynchronous Oscillations Caused by Wind Farms in Power Systems

Wenjuan Du , Member, IEEE, Qiang Fu , Haifeng Wang , Senior Member, IEEE, and Yang Wang 

Abstract—This paper investigates the torsional subsynchronous oscillations (SSOs) of synchronous generators caused by the grid-connected wind farms. The investigation does not rely on the representation of a wind farm by an aggregated wind generator and is based on a multi-input and multi-output closed-loop model. The model is comprised of the wind farm subsystem, which includes all the wind farms, and the subsystem of rest of power system (ROPS). Theoretical analysis proves that the open-loop SSO modal coupling of wind farm subsystem and ROPS subsystem results in the closed-loop SSO modal repulsion on the complex plane. Subsequently, damping of torsional SSOs decreases and growing SSOs may occur when the closed-loop modal repulsion is strong. Hence, closed-loop modal repulsion explains and reveals the mechanism about why the wind farms may cause the torsional SSOs in the power system. In addition, a method of open-loop modal analysis is proposed to detect the SSO instability risk brought about by the wind farms. The detection is based on the estimation of degree of closed-loop modal repulsion and only needs the modal information of open-loop subsystems. An example power system with wind farms is presented to demonstrate analysis and conclusions made in the paper.

Index Terms—Sub-synchronous oscillations, wind farms, modal analysis.

I. INTRODUCTION

SUBSYNCHRONOUS oscillation (SSOs) caused by grid-connected wind farms in a power system has been investigated intensively in recent years. It is presently one of major concerns of power system oscillations, which have threatened safe operation of modern power systems for years [1]–[17]. The investigation so far has focused on the following two main issues: (1) The mechanism about why a grid-connected wind farm may cause the SSOs; (2) Detection and suppression of under-damped or unstable SSOs caused by the wind farm [13]–[17].

Manuscript received February 1, 2018; revised June 13, 2018; accepted July 21, 2018. Date of publication August 3, 2018; date of current version December 19, 2018. This work was supported by the National Key Research and Development Program of China (No. 2016YFB0900602); and by the Technology Projects of State Grid Corporation of China (52094017000W). Paper no. TPWRS-00150-2018. (Corresponding author: Haifeng Wang.)

W. Du, Q. Fu, and H. Wang are with the State Key Laboratory of Alternate Electric Power Systems with New Energy Resources, North China Electric Power University, Beijing 102206, China (e-mail: ddwenjuan@qq.com; 1197348393@qq.com; hfwang60@qq.com).

Y. Wang is with the School of Electric and Electronic Engineering, North China Electric Power University, Beijing 102206, China (e-mail: wangyang_ncepu@126.com).

Color versions of one or more of the figures in this paper are available online at <http://ieeexplore.ieee.org>.

Digital Object Identifier 10.1109/TPWRS.2018.2862883

To study the first issue, both the frequency-domain analysis and modal analysis have been used.

The frequency-domain analysis [1]–[7] is usually based on the closed-loop impedance model, which is comprised of the wind farm subsystem and the subsystem of the rest of power system (ROPS). The analysis is to detect the SSO stability of the closed-loop model by using the frequency-domain information of the open-loop subsystems. Theoretical foundation for the detection is the Nyquist or passivity criterion. The frequency-domain analysis explains and attributes the SSO instability risk to the negative resistance contribution from the wind farm [1]–[7].

The Nyquist and passivity criteria are only simple and easily applicable for a single-input and single-output (SISO) closed-loop model. However, the output current from and terminal voltage of the wind farm normally should be expressed as vectors. The closed-loop impedance model is, in fact, multi-input and multi-output (MIMO). Hence, when the frequency-domain analysis was applied, a single wind generator was often used as the reduced-order aggregated representation of the wind farm. In addition, some further assumptions were made in order to derive the SISO closed-loop impedance model [1]–[7]. Simplifying the MIMO closed-loop model to the SISO closed-loop model for applying the frequency-domain analysis has brought about following two unsolved problems in studying the mechanism about why the wind farm may cause the SSOs: (1) Derivation of aggregated single wind generator to represent the wind farm for the SSO study; (2) Interpretation of conclusions obtained when the single wind generator was used for the case of wind farm.

From the viewpoint of practical applications, detection of SSO instability risk by using the information of open-loop subsystems is advantageous. This is because often the wind farms and the power system are of different owners and operators. For various commercial and technical reasons, it would be practically impossible to ask all the wind farms to hand over the complete and detailed data for establishing the model of entire power system with the wind farms in order to assess the system SSO instability risk. The frequency-domain analysis can identify the SSO instability risk by using the frequency characteristics of open-loop wind farm subsystem and hence is an application-oriented method.

The open-loop modal analysis was proposed on the basis of the closed-loop model of the power system with a wind farm in [10]–[12]. The SSO instability risk was detected by applying the modal analysis to the interconnected open-loop

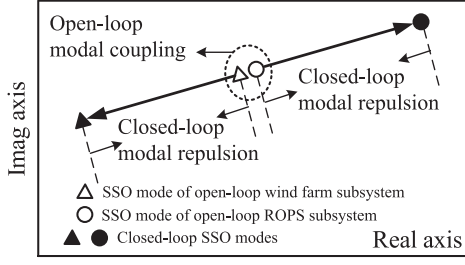


Fig. 1. Open-loop modal coupling to cause the closed-loop modal repulsion.

subsystems instead of the entire closed-loop system [10]–[12]. Theoretical foundation of open-loop modal analysis proposed in [10]–[12] was the open-loop modal coupling to result in closed-loop modal repulsion as illustrated by Fig. 1: Open-loop modal coupling was the closeness of an SSO mode of the open-loop wind farm subsystem to an SSO mode of the ROPS subsystem on the complex plane. Under the condition open-loop modal coupling, two closed-loop SSO modes corresponding to the coupled open-loop SSO modes are located at the positions opposite to each other in respect to the positions of coupled open-loop SSO modes. Hence, when the closed-loop modal repulsion was strong, poorly-damped or even growing SSOs may occur as caused by the wind farm. However, the closed-loop modal repulsion was only theoretically proved and validated on the basis of SISO closed-loop model [10]–[12]. Therefore, application of the open-loop modal analysis faces the same two unsolved problems mentioned beforehand for the application of frequency-domain analysis.

This paper examines the SSOs caused by the wind farms in a power system without using the single wind generators to represent the wind farms. The examination is based on the MIMO closed-loop model comprised of the wind farm subsystem and the ROPS subsystem. The correctness of open-loop modal coupling to cause the closed-loop modal repulsion in the MIMO closed-loop model is theoretically proved. Hence, the mechanism about why the wind farms may bring about the SSO instability risk is explained and revealed from the perspective of closed-loop modal repulsion.

In addition, estimation on the degree of closed-loop modal repulsion is derived for the MIMO closed-loop model in the paper. Based on the estimation, open-loop modal analysis is proposed to detect the SSO instability risk brought about by the wind farms. The detection only requires the wind farms to provide the open-loop modal information (the SSO modes and the associated residues), rather than the detailed data of every wind generators in the wind farms, for detecting the SSO instability risk. This makes the detection more applicable in practice.

An example power system with the wind farms is presented to validate the analysis and conclusions made in the paper. The open-loop modal coupling between the wind farms and the torsional dynamics of synchronous generators caused the closed-loop modal repulsion in the example power system, resulting in unstable SSOs. Study cases demonstrate how gain settings of converter control systems of individual wind generators and the

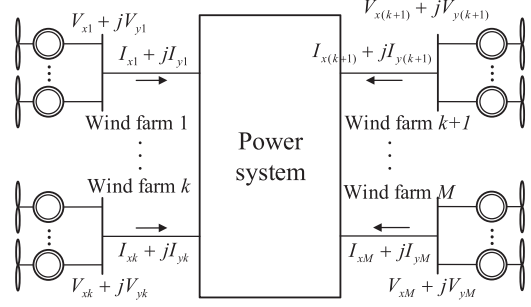


Fig. 2. A multi-machine power system with M wind farms.

number of grid-connected wind generators in the wind farms affect the close-loop modal repulsion in the example power system. They explain how the torsional SSOs may be affected by the factors associated with wind farms.

II. MODAL REPULSION CAUSED BY WIND FARMS

First, this section derives an MIMO closed-loop model for a power system with multiple wind farms. All the wind farms are modelled as the open-loop wind farm subsystem and the rest of power system (ROPS), excluding the wind farms, is modelled as the open-loop ROPS subsystem. Second, theoretical analysis is presented to indicate that when the open-loop modal coupling happens, i.e., an open-loop SSO mode of wind farm subsystem is close to an open-loop SSO mode of ROPS subsystem on the complex plane, closed-loop modal repulsion occurs to result in the damping decrease of the SSOs in the power system. Third, a method of open-loop modal analysis is proposed to detect the SSO instability risk brought about by the wind farms. Advantages of the proposed method are discussed.

A. MIMO Closed-Loop Model

Fig. 2 shows the configuration of a power system with M wind farms. Denote $I_{xk} + jI_{yk}$, $k = 1, 2, \dots, M$ as the output current from and $V_{xk} + jV_{yk}$, $k = 1, 2, \dots, M$ as the terminal voltage of the k th wind farm, both of which are expressed in the common $x - y$ coordinate of the power system. Following linearized transfer function matrix model of M wind farms can be established

$$\Delta \mathbf{I} = \mathbf{W}(s) \Delta \mathbf{V} \quad (1)$$

where prefix Δ indicates the small variation of a variable and

$$\begin{aligned} \Delta \mathbf{I} &= [\Delta I_{x1} \quad \Delta I_{y1} \quad \cdots \quad \Delta I_{xM} \quad \Delta I_{yM}]^T \\ \Delta \mathbf{V} &= [\Delta V_{x1} \quad \Delta V_{y1} \quad \cdots \quad \Delta V_{xM} \quad \Delta V_{yM}]^T. \end{aligned}$$

From (1), the state-space model of open-loop wind farm subsystem can be represented as

$$\begin{aligned} \frac{d}{dt} \Delta \mathbf{X}_W &= \mathbf{A}_W \Delta \mathbf{X}_W + \mathbf{B}_W \Delta \mathbf{V} \\ \Delta \mathbf{I} &= \mathbf{C}_W \Delta \mathbf{X}_W + \mathbf{D}_W \Delta \mathbf{V} \end{aligned} \quad (2)$$

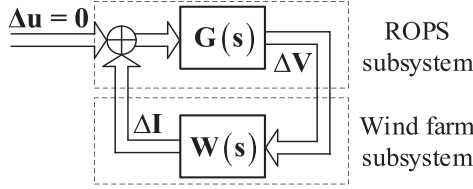


Fig. 3. MIMO closed-loop model.

where $\Delta \mathbf{X}_W$ is the vector of all the state variables of M wind farms and

$$\mathbf{W}(s) = \mathbf{C}_W(s\mathbf{I} - \mathbf{A}_W)^{-1}\mathbf{B}_W + \mathbf{D}_W \quad (3)$$

The rest of power system (ROPS) in Fig. 2, excluding the dynamics of M wind farms, can be described by the following transfer function matrix model

$$\Delta \mathbf{V} = \mathbf{G}(s)\Delta \mathbf{I} \quad (4)$$

From (4), the state-space model of the open-loop ROPS subsystem can be written as

$$\begin{aligned} \frac{d}{dt}\Delta \mathbf{X}_A &= \mathbf{A}_A\Delta \mathbf{X}_A + \mathbf{B}_A\Delta \mathbf{I} \\ \Delta \mathbf{V} &= \mathbf{C}_A\Delta \mathbf{X}_A + \mathbf{D}_A\Delta \mathbf{I} \end{aligned} \quad (5)$$

where $\Delta \mathbf{X}_A$ is the vector of all the state variables of the open-loop ROPS subsystem and

$$\mathbf{G}(s) = \mathbf{C}_A(s\mathbf{I} - \mathbf{A}_A)^{-1}\mathbf{B}_A + \mathbf{D}_A \quad (6)$$

From (1) and (4), an MIMO closed-loop model of the power system with the wind farms is obtained and shown by Fig. 3. The state-space representation of closed-loop model shown by Fig. 3 is obtained from (2) and (5) to be

$$\frac{d}{dt}\Delta \mathbf{X} = \mathbf{A}\Delta \mathbf{X} = \begin{bmatrix} \mathbf{A}_{11} & \mathbf{A}_{12} \\ \mathbf{A}_{21} & \mathbf{A}_{22} \end{bmatrix} \Delta \mathbf{X} \quad (7)$$

where

$$\begin{aligned} \Delta \mathbf{X} &= [\Delta \mathbf{X}_A^T \quad \Delta \mathbf{X}_W^T]^T \\ \mathbf{A}_{11} &= \mathbf{A}_A + \mathbf{B}_A\mathbf{D}_W(\mathbf{I} - \mathbf{D}_A\mathbf{D}_W)^{-1}\mathbf{C}_A \\ \mathbf{A}_{12} &= \mathbf{B}_A\mathbf{C}_W + \mathbf{B}_A\mathbf{D}_W(\mathbf{I} - \mathbf{D}_A\mathbf{D}_W)^{-1}\mathbf{D}_A\mathbf{C}_W \\ \mathbf{A}_{21} &= \mathbf{B}_W(\mathbf{I} - \mathbf{D}_A\mathbf{D}_W)^{-1}\mathbf{C}_A \\ \mathbf{A}_{22} &= \mathbf{A}_W + \mathbf{B}_W(\mathbf{I} - \mathbf{D}_A\mathbf{D}_W)^{-1}\mathbf{D}_A\mathbf{C}_W \end{aligned}$$

B. Close-Loop Modal Repulsion

Denote λ_a and λ_w as an open-loop SSO mode of the ROPS subsystem and wind farm subsystem in Fig. 3 respectively. λ_a is a complex eigenvalue of open-loop state matrix \mathbf{A}_A in (5) and λ_w is a complex eigenvalue of open-loop state matrix \mathbf{A}_W in (2). When the closed-loop model shown by Fig. 3 is single-input and single-output (SISO), the modal condition that λ_a and λ_w are close to each other on the complex plane, i.e., $\lambda_a \approx \lambda_w$, was referred to as the open-loop modal coupling in [10]–[12].

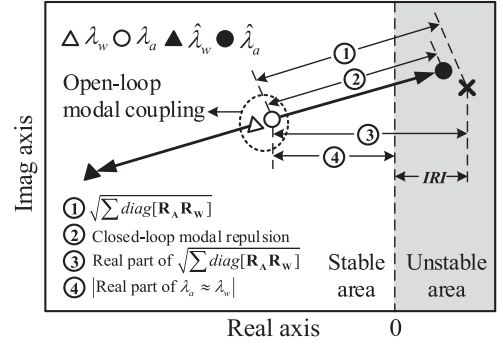


Fig. 4. Closed-loop modal repulsion.

Denote $\hat{\lambda}_a$ and $\hat{\lambda}_w$ as the closed-loop SSO modes corresponding to λ_a and λ_w . $\hat{\lambda}_a$ and $\hat{\lambda}_w$ are the complex eigenvalues of closed-loop state matrix \mathbf{A} in (7). When Fig. 3 is the SISO closed-loop model, it was proved in [10]–[12] that under the condition of open-loop modal coupling, i.e., $\lambda_a \approx \lambda_w$, $\hat{\lambda}_a$ and $\hat{\lambda}_w$ are located at the approximately opposite positions on the complex plane with respect to the coupled open-loop SSO modes, $\lambda_a \approx \lambda_w$. The proof was conducted by deriving the estimation of $\hat{\lambda}_a$ and $\hat{\lambda}_w$. Hence, to extend the concept of closed-loop modal repulsion to the MIMO closed-loop model shown by Fig. 3, estimation of $\hat{\lambda}_a$ and $\hat{\lambda}_w$ is derived as follows.

Denote \mathbf{w}_w and \mathbf{v}_w as the left and right eigenvector of open-loop state matrix \mathbf{A}_W in (2) for λ_w . Following residue matrix for the wind farm subsystem is defined

$$\mathbf{R}_W = (\mathbf{C}_W\mathbf{v}_w)(\mathbf{w}_w^T\mathbf{B}_W) \quad (8)$$

Denote \mathbf{w}_a and \mathbf{v}_a as the left and right eigenvector of open-loop state matrix \mathbf{A}_A in (5) for λ_a . Following residue matrix for the ROPS subsystem is defined

$$\mathbf{R}_A = (\mathbf{C}_A\mathbf{v}_a)(\mathbf{w}_a^T\mathbf{B}_A) \quad (9)$$

It is proved in Appendix that when $\lambda_a \approx \lambda_w$,

$$\begin{aligned} \hat{\lambda}_a &\approx \lambda_a \pm \sqrt{\sum \text{diag}[\mathbf{R}_A\mathbf{R}_W]} \\ \hat{\lambda}_w &\approx \lambda_w \pm \sqrt{\sum \text{diag}[\mathbf{R}_A\mathbf{R}_W]} \approx \lambda_a \\ &\quad \pm \sqrt{\sum \text{diag}[\mathbf{R}_A\mathbf{R}_W]} \end{aligned} \quad (10)$$

where $\text{diag}[\]$ refers to the diagonal elements of a matrix.

From (10), it can be seen that $\hat{\lambda}_a$ and $\hat{\lambda}_w$ are located at the approximately opposite positions on the complex plane with respect to the coupled open-loop SSO modes, $\lambda_a \approx \lambda_w$. This is the closed-loop modal repulsion as illustrated by Fig. 4. It can be seen that the degree of closed-loop modal repulsion can be estimated by the following instability risk index (IRI)

$$\begin{aligned} \text{IRI} &= \left| \text{Real part of } \sqrt{\sum \text{diag}[\mathbf{R}_A\mathbf{R}_W]} \right| \\ &\quad - |\text{Real part of } \lambda_a \approx \lambda_w| \end{aligned} \quad (11)$$

If IRI is positive, either $\hat{\lambda}_a$ and $\hat{\lambda}_w$ may be located on the right half of complex plane such that growing SSOs occur in the power system.

Analysis presented above about the open-loop modal coupling to cause the closed-loop modal repulsion explains and reveals the mechanism about why the SSO instability risk may be brought about by the wind farms. In addition, a method of open-loop modal analysis can be proposed by using the proposed IRI . The method is introduced in the following subsection.

C. Method of Open-Loop Modal Analysis

Steps of the proposed method of open-loop modal analysis are summarized as follows.

- (1) Establish the models of the open-loop wind farm subsystem and the ROPS subsystem shown in Fig. 3.
- (2) Compute the open-loop SSO modes of the wind farm subsystem and the ROPS subsystem. Identify any open-loop modal coupling. For example, $\lambda_a \approx \lambda_w$ is identified.
- (3) For the identified open-loop modal coupling, $\lambda_a \approx \lambda_w$, calculate the residue matrices defined in (8) and (9). Calculate IRI index defined in (11). Positive IRI indicates the SSO instability risk introduced by the grid connection of the wind farms.

The method of open-loop modal analysis outlined above is computationally advantageous as to be explained as follows.

In the power system shown by Fig. 2, M wind farms can be considered being connected to M different points of common coupling (PCC), because if two wind farms are connected to a same PCC, they can be treated as one wind farm. Hence, the transfer function matrix of wind farm subsystem in (1) is a diagonal block matrix, i.e.,

$$\Delta \mathbf{I} = \text{diag}[\mathbf{W}_k(s)] \Delta \mathbf{V} \quad (12)$$

where

$$\begin{aligned} \Delta \mathbf{I} &= [\Delta \mathbf{I}_1 \quad \Delta \mathbf{I}_2 \quad \cdots \quad \Delta \mathbf{I}_M], \\ \Delta \mathbf{V} &= [\Delta \mathbf{V}_1 \quad \Delta \mathbf{V}_2 \quad \cdots \quad \Delta \mathbf{V}_M] \\ \Delta \mathbf{I}_k &= \mathbf{W}_k(s) \Delta \mathbf{V}_k, \quad \Delta \mathbf{I}_k = [\Delta I_{xk} \quad \Delta I_{yk}]^T, \\ \Delta \mathbf{V}_k &= [\Delta V_{xk} \quad \Delta V_{yk}]^T \end{aligned}$$

and $k = 1, 2, \dots, M$. Thus, the matrices in the state-space model of wind farm subsystem are all diagonal block matrices, i.e.,

$$\begin{aligned} \mathbf{A}_W &= \text{diag}[\mathbf{A}_k], \mathbf{B}_W = \text{diag}[\mathbf{B}_k], \\ \mathbf{C}_W &= \text{diag}[\mathbf{C}_k], \mathbf{D}_W = \text{diag}[\mathbf{D}_k] \end{aligned} \quad (13)$$

If λ_w is an SSO mode of the k th wind farm and the eigenvalue of \mathbf{A}_k with the associated left and right eigenvector respectively to be \mathbf{w}_k and \mathbf{v}_k , λ_w is also the eigenvalue of \mathbf{A}_W with the associated left and right eigenvector respectively to be

$$\begin{aligned} \mathbf{v}_w &= [\mathbf{0} \quad \cdots \quad \mathbf{v}_k \quad \mathbf{0} \quad \cdots]^T, \\ \mathbf{w}_w^T &= [\mathbf{0} \quad \cdots \quad \mathbf{w}_k^T \quad \mathbf{0} \quad \cdots] \end{aligned} \quad (14)$$

Hence, λ_w is an SSO mode of wind farm subsystem and the associated residue matrix defined in (8) is

$$\mathbf{R}_W = \text{diag} [\mathbf{0} \quad \cdots \quad (\mathbf{C}_k \mathbf{v}_k)(\mathbf{w}_k^T \mathbf{B}_k) \quad \mathbf{0} \quad \cdots] \quad (15)$$

Therefore, the modal analysis for the wind farm subsystem (computation of SSO modes and the residue matrix) to detect the SSO instability risk can be carried out for EACH of M wind farms, instead of the entire M wind farms. Thus, the dimension of matrices involved in the eigensolution to conduct the open-loop modal analysis is irrelevant with the number of wind farms in the power system. This is very computational convenient.

For example, assume that in an L -machine power system with M wind farms, the average order of dynamic model of a synchronous generator is 20, that of a wind generator is 13 and there are 50 wind generators in a wind farm. The dimension of the closed-loop state matrix of the entire L -machine power system with M wind farms is $20 \times L + 13 \times 50 \times M$ (Other dynamic components are not considered). Conventional method of modal analysis applied to the entire power system will meet the numerical difficulty when the number of wind farms in the power system is more than 20. Whilst, the dimensions of state matrices involved in the open-loop modal analysis are $20 \times L$ for the open-loop ROPS subsystem and $13 \times 50 = 650$ for each of the wind farm, which is irrelevant with M , the number of wind farms.

Consider the fact that the capacity of wind generators is relatively small. Thus, in a power system with high penetration of wind power, the number of wind farms and wind generators will be very high, which could cause the numerical problem for the eigensolution of closed-loop state matrix of entire power system when the conventional modal analysis is applied. Hence, the open-loop modal analysis is computationally advantageous as compared with the conventional modal analysis.

From the viewpoint of practical application, modal information of open-loop wind farm subsystem and the ROPS subsystem may be obtained by applying the modal identification algorithms. Thus, SSO instability risk may be detected by the modal identification technique from the field measurement data rather than the parametric models, as the frequency-domain analysis can do. Further work is needed to develop and validate such technique. The concept of closed-loop modal repulsion and method of open-loop modal analysis presented above in this section has established the theoretical foundation for the development of measurement based technique to detect the SSO instability risk brought about by the wind farms.

In the next section, an example power system with two wind farms is presented to demonstrate and evaluate the analysis and conclusions. The open-loop modal coupling to cause the closed-loop modal repulsion between the wind farms and the torsional dynamics of synchronous generators are demonstrated. How the gain setting of converter control systems and the number of grid-connected wind generators in the wind farms affect the SSOs is examined. Such examination is not possible if the aggregated representation of wind farms by wind generators is used.

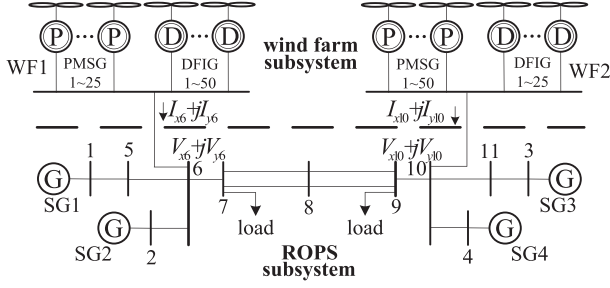


Fig. 5. Configuration of first example power system with two wind farms.

III. AN EXAMPLE POWER SYSTEM

A. The Example Power System

Fig. 5 shows the configuration of an example power system [18] with two wind farms being connected at node 6 and node 10 respectively. There were 50 DFIGs and 25 PMSGs in the first wind farm (WF1) at node 6. The second wind farm (WF2) was comprised of 50 PMSGs and 25 DFIGs. Parameters of the power system given in [18] were used. The model and parameters of synchronous generators recommended in the IEEE first benchmark power system for the SSR study in [19] were adopted with parameters being adjusted according to the capacity of synchronous generators. Models and parameters of the DFIGs and PMSGs given in [8] and [19] were used respectively.

The example power system was divided into the wind farm subsystem and the ROPS subsystem. The wind farm subsystem included WF1 and WF2. The ROPS subsystem was comprised of the AC power system. Interface variables between two subsystems were output current and terminal voltage at node 6 and node 10. The state-space model of open-loop subsystems described by (2) and (5) were established with

$$\Delta \mathbf{I} = [\Delta I_{x6} \quad \Delta I_{y6} \quad \Delta I_{x10} \quad \Delta I_{y10}]^T$$

$$\Delta \mathbf{V} = [\Delta V_{x6} \quad \Delta V_{y6} \quad \Delta V_{x10} \quad \Delta V_{y10}]^T$$

Open-loop modal analysis was applied to detect the SSO instability risk brought about by the wind farms as presented in the following two subsections.

B. The Closed-Loop Modal Repulsion Between the Wind Farms and the Torsional Dynamics of Synchronous Generators

First, the open-loop SSO modes of ROPS subsystem were computed from the open-loop state matrix \mathbf{A}_A given in (5). The computational results of the first and second torsional SSO modes of synchronous generators of ROPS subsystem are presented in Table I.

Second, the open-loop SSO modes of wind farm subsystem were calculated from the open-loop state matrix \mathbf{A}_W defined in (2). It was found that WF1 had an open-loop SSO mode, $\lambda_{w1} = -0.75 + j94.8$, which was very close to the 1st open-loop torsional SSO mode of SG2, $\lambda_{a1} = -0.21 + j94.8$. In addition, WF2 was of an open-loop SSO mode, $\lambda_{w2} = -0.29 + j105.1$, which was very close to the 1st open-loop torsional SSO mode of SG4, $\lambda_{a2} = -0.21 + j104.9$. Thus, $\lambda_{w1} \approx \lambda_{a1}$ and $\lambda_{w2} \approx \lambda_{a2}$ were identified as two cases of open-loop modal coupling.

TABLE I
COMPUTATION RESULTS OF OPEN-LOOP SSO MODES OF ROPS SUBSYSTEM

The 1 st and 2 nd open-loop torsional SSO modes of synchronous generators	Relation of the 1 st and 2 nd open-loop torsional SSO modes with the synchronous generators
$-0.66 + j133.9$	The 2 st torsional SSO mode of SG4
$-0.66 + j127.0$	The 2 st torsional SSO mode of SG3
$-0.66 + j121.1$	The 2 st torsional SSO mode of SG2
$-0.66 + j116.0$	The 2 st torsional SSO mode of SG1
$\lambda_{a2} = -0.21 + j104.9$	The 1 st torsional SSO mode of SG4
$-0.18 + j99.3$	The 1 st torsional SSO mode of SG3
$\lambda_{a1} = -0.21 + j94.8$	The 1 st torsional SSO mode of SG2
$\lambda_{a3} = -0.19 + j90.5$	The 1 st torsional SSO mode of SG1

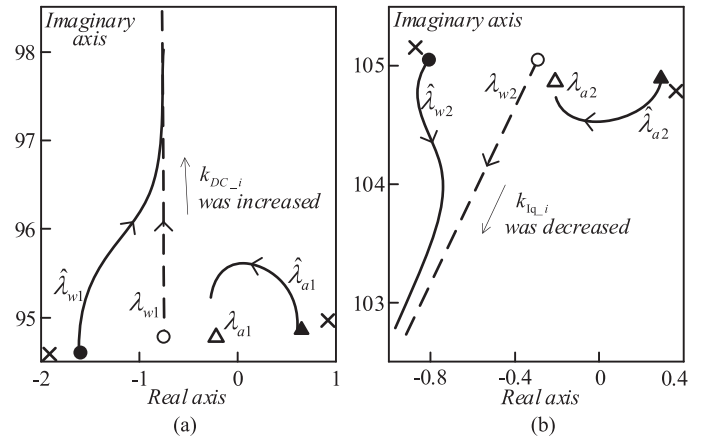


Fig. 6. Modal trajectories to evaluate the closed-loop modal repulsion and improvement of the SSO stability by gain tuning of converter control systems of the DFIGs in WF1 and WF2.

Third, IRI defined in (11) was calculated for the identified cases of open-loop modal coupling. For $\lambda_{w1} \approx \lambda_{a1}$, $\sqrt{\sum \text{diag}[\mathbf{R}_A \mathbf{R}_W]} = 1.16 + j0.22$ such that $IRI = 0.95 > 0$. Hence, identified open-loop modal coupling between WF1 and SG2, $\lambda_{w1} \approx \lambda_{a1}$, was expected to cause growing torsional SSOs in the example power system. For $\lambda_{w2} \approx \lambda_{a2}$, $\sqrt{\sum \text{diag}[\mathbf{R}_A \mathbf{R}_W]} = 0.58 - j0.07$ such that $IRI = 0.37 > 0$. Identified open-loop modal coupling between WF2 and SG4, $\lambda_{w2} \approx \lambda_{a2}$, was also anticipated to result in unstable torsional SSOs in the example power system.

Closed-loop SSO modes corresponding to λ_{w1} and λ_{a1} were $\hat{\lambda}_{w1}$ and $\hat{\lambda}_{a1}$. In Fig. 6(a), positions of λ_{w1} and λ_{a1} on the complex plane are indicated by hollow circle and triangle respectively. Positions of $\hat{\lambda}_{w1}$ and $\hat{\lambda}_{a1}$ estimated by using (10) are indicated by crosses. It can be seen that $\hat{\lambda}_{w1}$ and $\hat{\lambda}_{a1}$ were located at the opposite positions to each other in respect to the positions of $\lambda_{w1} \approx \lambda_{a1}$, confirming the occurrence of closed-loop modal repulsion under the condition of open-loop modal coupling, $\lambda_{w1} \approx \lambda_{a1}$. For confirmation, $\hat{\lambda}_{w1}$ and $\hat{\lambda}_{a1}$ were calculated by using the closed-loop state matrix \mathbf{A} given in (7). Their positions on the complex plane are indicated by the filled circle and triangle respectively in Fig. 6 (a), confirming the correctness of (10) and the prediction of system SSO instability risk made by the above open-loop modal analysis.

Damping decrease of $\hat{\lambda}_{a1}$ was due to the closed-loop modal repulsion under the condition of open-loop modal coupling, $\lambda_{w1} \approx \lambda_{a1}$. By eliminating the identified open-loop modal coupling, $\lambda_{w1} \approx \lambda_{a1}$, damping of $\hat{\lambda}_{a1}$ can be enhanced. Hence, participation factors for $\lambda_{w1} = -0.75 + j94.8$ were computed. Computational results indicated that λ_{w1} was related to the DC voltage control outer loops of the grid side converter (GSC) of the DFIGs in WF1. Hence, the integral gains of the DC voltage control outer loops, k_{DC-i} , were tuned from $k_{DC-i} = 1.31$ to $k_{DC-i} = 1.41$. Trajectory of λ_{w1} with k_{DC-i} being tuned is displayed in Fig. 6(a) as dashed curve. It can be seen that tuning k_{DC-i} moved λ_{w1} away from λ_{a1} such that the open-loop modal coupling, $\lambda_{w1} \approx \lambda_{a1}$, was eliminated.

In Fig. 6(a), trajectories of $\hat{\lambda}_{w1}$ and $\hat{\lambda}_{a1}$ with k_{DC-i} being tuned are displayed as solid curves. It confirmed that with k_{DC-i} being tuned, $\hat{\lambda}_{a1}$ moved towards left and its damping was improved. When $k_{DC-i} = 1.41$, $\hat{\lambda}_{a1}$ was located in the left half of complex plane.

For the identified open-loop modal coupling, $\lambda_{w2} \approx \lambda_{a2}$, the closed-loop modal repulsion is demonstrated in Fig. 6(b). It was found that λ_{w2} was related to the q-axis current control inner loops of the grid side converter (GSC) of the DFIGs in WF2. Hence, by tuning the integral gains of the q-axis current control inner loops, k_{Iq-i} , from $k_{Iq-i} = 9.66$ to $k_{Iq-i} = 9$, open-loop modal coupling, $\lambda_{w2} \approx \lambda_{a2}$, was eliminated. Subsequently, damping of $\hat{\lambda}_{a2}$ was enhanced. When $k_{Iq-i} = 9$, $\hat{\lambda}_{a2}$ was located in the left half of complex plane, as shown in Fig. 6(b).

Confirmation from non-linear simulation is presented in Fig. 7. At 0.01 second of simulation, 10% of load at node 9 was lost for 100 ms. Following two cases were simulated: (1) $k_{DC-i} = 1.31$ and $k_{Iq-i} = 9$ when the closed-loop modal repulsion between WF1 and SG2 (when $\lambda_{w1} \approx \lambda_{a1}$) caused the growing torsional SSOs. In this case, $\hat{\lambda}_{a1}$ was on the right half of complex plane, but $\hat{\lambda}_{a2}$ was on the left half. (2) $k_{DC-i} = 1.41$ and $k_{Iq-i} = 9.66$ when the closed-loop modal repulsion between WF2 and SG4 (when $\lambda_{w2} \approx \lambda_{a2}$) caused the unstable torsional SSOs. In this case, $\hat{\lambda}_{a1}$ was on the left half of complex plane, but $\hat{\lambda}_{a2}$ was on the right half.

C. Closed-Loop Modal Repulsion Affected by the Number of Grid-Connected Wind Generators in the Wind Farm

In Fig. 6(a), open-loop modal coupling, $\lambda_{w1} \approx \lambda_{a1}$, happened when the integral gain of DC voltage control of the GSC of all 50 DFIGs in WF1 was set to be $k_{DC-i} = 1.31$. To examine the impact of closed-loop modal repulsion as affected by the number of the DFIGs taking part in the open-loop modal coupling, initially the integral gains of DC voltage control of the GSC of all 50 DFIGs were set to be $k_{DC-i} = 1.41$ such that the open-loop modal coupling was dismissed as shown in Fig. 6(a). Then, the integral gains of various number (N) of the DFIGs were gradually decreased to $k_{DC-i} = 1.31$. Modal trajectories with the integral gain being tuned in this way are displayed in Fig. 8. It can be seen that the degree of closed-loop modal repulsion increased with more DFIGs getting involved in the open-loop modal coupling. This implied that if the SSO instability was caused by the closed-loop modal repulsion, it was very

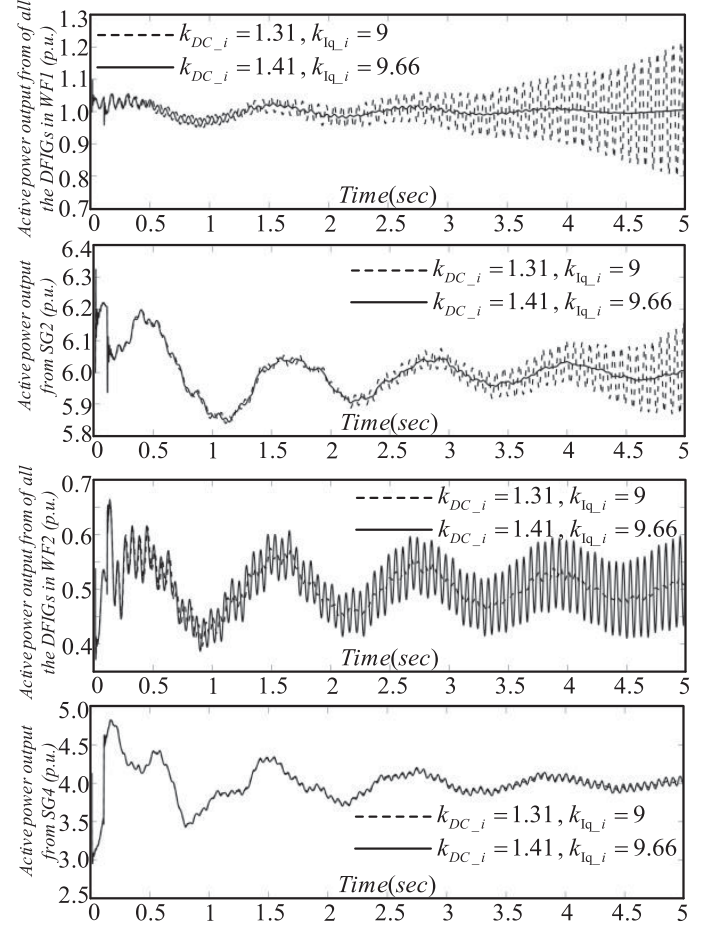


Fig. 7. Results of non-linear simulation.

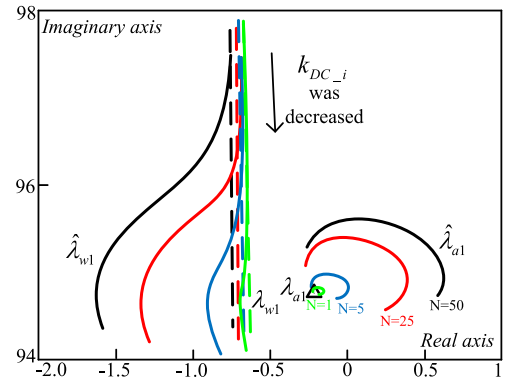


Fig. 8. Modal trajectories to evaluate the degree of closed-loop modal repulsion affected the number (N) of the grid-connected DFIGs in WF1.

likely that many wind generators in the wind farm got involved. For example, it can be noted that the degree of closed-loop modal repulsion was very small when $N = 1$ (one DFIG was involved in the open-loop modal coupling), causing little damping degradation of $\hat{\lambda}_{a1}$. In other words, tuning control parameters of only a couple of DFIGs may very possibly not be able to stabilize the growing SSOs caused by the closed-loop modal repulsion.

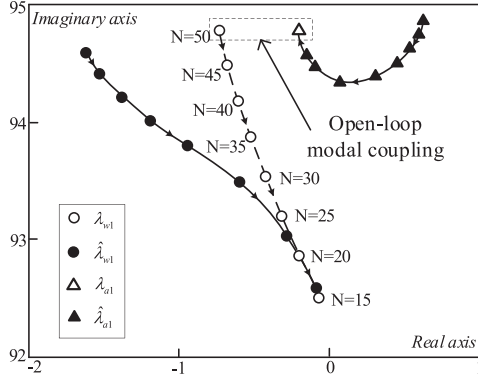


Fig. 9. Modal trajectories when the number of grid-connected DFIGs in WF1 was reduced from 50 to 15.

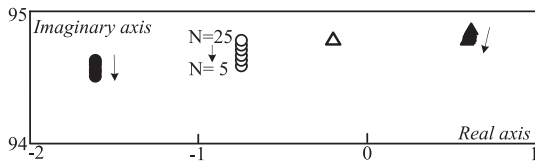


Fig. 10. Modal trajectories when the number of grid-connected PMSGs in WF1 was reduced from 25 to 5.

Under the condition of open-loop modal coupling, $\lambda_{w1} \approx \lambda_{a1}$, number of grid-connected DFIGs (N) was reduced from 50 to 15. Modal trajectories are presented in Fig. 9. It can be seen that with more and more DFIGs being disconnected from the grid, the open-loop SSO mode of WF1 moved on the complex plane from $\lambda_{w1} = -0.75 + j94.8$ to $\lambda_{w1} = -0.07 + j92.5$. Open-loop torsional SSO mode of SG2, λ_{a1} , was not affected and its position was not changed. Thus, disconnection of DFIGs gradually dismissed the condition of open-loop modal coupling ($\lambda_{w1} \approx \lambda_{a1}$) such that closed-loop torsional SSO mode, $\hat{\lambda}_{a1}$, moved from $\hat{\lambda}_{a1} = 0.62 + j94.9$ to $\hat{\lambda}_{a1} = -0.16 + j94.58$ with improved damping.

From Fig. 9, it can also be noted that increase of number of grid-connected DFIGs in WF1, for example from $N = 15$ to $N = 50$, resulted in the open-loop modal coupling to lead to the growing SSOs in the power system. It was due to the movement of open-loop SSO mode of WF1 on the complex plane as caused by the increase of number of grid-connected DFIGs in WF1.

When the number of grid-connected PMSGs (N), instead of the DFIGs, in WF1 was reduced from 25 to 5, modal trajectories are displayed in Fig. 10. It can be seen that change of number of grid-connected PMSGs affected very little the condition of open-loop modal coupling. This result confirmed that the open-loop modal coupling was the key reason of the SSOs caused by WF1, when the number of grid-connected wind generators varied. Change of number of grid-connected wind generators

in the wind farm may not affect the damping of the SSOs in the power system caused by the wind farm if the condition of open-loop modal coupling is not affected.

IV. CONCLUSIONS

In a power system with multiple wind farms, division of the power system into the wind farm subsystem and ROPS subsystem results in a MIMO closed-loop model. It has been a challenging task to detect the SSO instability risk brought about by the wind farms from the information of open-loop subsystems when the MIMO closed-loop model was used.

This paper has studied the SSOs caused by multiple wind farms in the power system without representing the wind farms by the single wind generators. Hence, the study has been based on the MIMO closed-loop model. Theoretical analysis in the paper has proved that in the MIMO closed-loop model, the open-loop modal coupling causes the closed-loop modal repulsion. When the closed-loop modal repulsion is strong, growing SSOs occur in the power system as caused by the grid connection of wind farms. Hence, main contribution of the paper is the revelation of the mechanism about why the wind farms may bring about the SSO instability risk in the power system. In addition, estimation of closed-loop SSO modes by using the modal information of open-loop subsystems is derived for the MIMO closed-loop model. Method of open-loop modal analysis has been proposed to detect the SSO instability risk brought about by the wind farms. The method is computational advantageous because the dimension of matrices involved in the eigensolution does not increase with the increase of number of wind farms in the power system.

APPENDIX

Physical exhibitions of the dynamic interactions between the wind farms and the power system are the variations of current outputs of the wind farms, $\Delta I_{xk} + j\Delta I_{yk}$, $k = 1, 2, \dots, M$. Normally, the dynamic interactions are weak due to the fast speed of converter control implemented by the wind generators in the wind farms such that $\Delta I_{xk} + j\Delta I_{yk} \approx 0$, $k = 1, 2, \dots, M$. To depict the weak dynamic interactions between the wind farms and the power system, a small positive number, $0 < \varepsilon \ll 1$, is introduced to express (1) as

$$\Delta \mathbf{I} = \mathbf{W}(s)\Delta \mathbf{V} = \varepsilon \mathbf{H}(s)\Delta \mathbf{V} \quad (A1)$$

The state-space model of the open-loop wind farm subsystem shown by (2) can be written as

$$\begin{aligned} \frac{d}{dt}\Delta \mathbf{X}_W &= \mathbf{A}_W \Delta \mathbf{X}_W + \mathbf{B}_W \Delta \mathbf{V} \\ \Delta \mathbf{I} &= \mathbf{C}_W \Delta \mathbf{X}_W + \mathbf{D}_W \Delta \mathbf{V} = \varepsilon \mathbf{C}_H \Delta \mathbf{X}_W + \varepsilon \mathbf{D}_H \Delta \mathbf{V} \end{aligned} \quad (A2)$$

$$\mathbf{A}(\varepsilon) = \begin{bmatrix} \mathbf{A}_A + \varepsilon \mathbf{B}_A \mathbf{D}_H (\mathbf{I} - \varepsilon \mathbf{D}_A \mathbf{D}_H)^{-1} \mathbf{C}_A & \varepsilon \mathbf{B}_A \mathbf{C}_H + \varepsilon^2 \mathbf{B}_A \mathbf{D}_H (\mathbf{I} - \varepsilon \mathbf{D}_A \mathbf{D}_H)^{-1} \mathbf{D}_A \mathbf{C}_H \\ \mathbf{B}_W (\mathbf{I} - \varepsilon \mathbf{D}_A \mathbf{D}_H)^{-1} \mathbf{C}_A & \mathbf{A}_W + \varepsilon \mathbf{B}_W (\mathbf{I} - \varepsilon \mathbf{D}_A \mathbf{D}_H)^{-1} \mathbf{D}_A \mathbf{C}_H \end{bmatrix} \quad (A3)$$

From (A2), the closed-loop state matrix given in (7) can be written as (A3) shown at the bottom of the previous page.

When $\varepsilon = 0$, the above state matrix becomes

$$\mathbf{A}(0) = \begin{bmatrix} \mathbf{A}_A & \mathbf{0} \\ \mathbf{B}_W \mathbf{C}_A & \mathbf{A}_W \end{bmatrix} \quad (\text{A4})$$

The characteristic equation of the MIMO closed-loop interconnected system shown by Fig. 3 is

$$\text{Det}[\mathbf{I} - \mathbf{W}(s)\mathbf{G}(s)] = 0 \quad (\text{A5})$$

where $\text{Det}[\]$ refers to the determinant of a matrix. From (A1) and (A5),

$$\text{Det}[\mathbf{I} - \varepsilon \mathbf{H}(s)\mathbf{G}(s)] = 0 \quad (\text{A6})$$

Without loss of generality, let

$$\mathbf{G}(s) = \frac{\mathbf{g}(s)}{s - \lambda_a}, \mathbf{H}(s) = \frac{\mathbf{h}(s)}{s - \lambda_w} \quad (\text{A7})$$

Substituting (A7) in (A6),

$$\text{Det} \left[\mathbf{I} - \frac{(s - \lambda_a)(s - \lambda_w)}{\varepsilon} \mathbf{h}(s)\mathbf{g}(s) \right] = 0 \quad (\text{A8})$$

The above equation can be written as

$$\left[\frac{(s - \lambda_a)(s - \lambda_w)}{\varepsilon} \right]^{2M} + a_{2M-1}(s) \left[\frac{(s - \lambda_a)(s - \lambda_w)}{\varepsilon} \right]^{2M-1} + \dots + a_1(s) \frac{(s - \lambda_a)(s - \lambda_w)}{\varepsilon} + a_0(s) = 0 \quad (\text{A9})$$

Note that the order of polynomial in (A9) may not necessarily be $4M$, because $a_{2M-1}(s), \dots, a_1(s), a_0(s)$ are all polynomials.

Multiplying both sides of (A9) by $\frac{\varepsilon^{2M}}{[(s - \lambda_a)(s - \lambda_w)]^{2M-1}}$,

$$(s - \lambda_a)(s - \lambda_w) + a_{2M-1}(s)\varepsilon + \frac{a_{2M-2}(s)}{(s - \lambda_a)(s - \lambda_w)}\varepsilon^2 + \dots + \frac{a_1(s)\varepsilon^{2M-1}}{[(s - \lambda_a)(s - \lambda_w)]^{2M-2}} + \frac{a_0(s)\varepsilon^{2M}}{[(s - \lambda_a)(s - \lambda_w)]^{2M-1}} = 0 \quad (\text{A10})$$

Let

$$f_0(s) = (s - \lambda_a)(s - \lambda_w), f_1(s) = a_{2M-1}(s) \\ f_2(s) = \frac{a_{2M-2}(s)}{(s - \lambda_a)(s - \lambda_w)} + \dots + \frac{a_1(s)\varepsilon^{2M-3}}{[(s - \lambda_a)(s - \lambda_w)]^{2M-2}} \\ + \frac{a_0(s)\varepsilon^{2M-2}}{[(s - \lambda_a)(s - \lambda_w)]^{2M-1}} \quad (\text{A11})$$

With (A11), the characteristic equation of (A10) becomes

$$f_0(s) + \varepsilon f_1(s) + \varepsilon^2 f_2(s) = 0 \quad (\text{A12})$$

$\hat{\lambda}_a = \lambda_a + \Delta\lambda_a$ is a solution of the characteristic equation of (A12). Hence,

$$f_0(\lambda_a + \Delta\lambda_a) + \varepsilon f_1(\lambda_a + \Delta\lambda_a) + \varepsilon^2 f_2(\lambda_a + \Delta\lambda_a) = 0 \quad (\text{A13})$$

Taylor series expansion of (A13) at λ_a is

$$f_0(\lambda_a) + f_0'(\lambda_a)\Delta\lambda_a + \frac{f_0''(\lambda_a)}{2!}\Delta\lambda_a^2 \dots + \varepsilon f_1(\lambda_a) \\ + \varepsilon f_1'(\lambda_a)\Delta\lambda_a + \varepsilon \frac{f_1''(\lambda_a)}{2!}\Delta\lambda_a^2 \dots + \varepsilon^2 f_2(\lambda_a) \\ + \varepsilon^2 f_2'(\lambda_a)\Delta\lambda_a + \varepsilon^2 \frac{f_2''(\lambda_a)}{2!}\Delta\lambda_a^2 \dots = 0 \quad (\text{A14})$$

Since ε is a small positive number and when $\lambda_a = \lambda_w$, λ_a is the double eigenvalue of state matrix $\mathbf{A}(0)$ given in (A4). The small increment of λ_a is caused by variation from $\varepsilon = 0$ to ε which is a small number. Hence $\Delta\lambda_a$ can be expressed as [21]

$$\Delta\lambda_a = \beta_1 \varepsilon^{\frac{1}{2}} + \beta_2 \varepsilon^{\frac{2}{2}} + \beta_3 \varepsilon^{\frac{3}{2}} + \dots \quad (\text{A15})$$

where $\beta_k, k = 1, 2, \dots$ are a series of coefficients. Substitute (A15) in (A14),

$$f_0(\lambda_a) + f_0'(\lambda_a)(\beta_1 \varepsilon^{\frac{1}{2}} + \beta_2 \varepsilon^{\frac{2}{2}} + \beta_3 \varepsilon^{\frac{3}{2}} + \dots) + \frac{f_0''(\lambda_a)}{2!} \\ \times (\beta_1 \varepsilon^{\frac{1}{2}} + \beta_2 \varepsilon^{\frac{2}{2}} + \beta_3 \varepsilon^{\frac{3}{2}} + \dots)^2 \dots + \varepsilon f_1(\lambda_a) \\ + \varepsilon f_1'(\lambda_a)(\beta_1 \varepsilon^{\frac{1}{2}} + \beta_2 \varepsilon^{\frac{2}{2}} + \beta_3 \varepsilon^{\frac{3}{2}} + \dots) + \varepsilon \frac{f_1''(\lambda_a)}{2!} \\ (\beta_1 \varepsilon^{\frac{1}{2}} + \beta_2 \varepsilon^{\frac{2}{2}} + \beta_3 \varepsilon^{\frac{3}{2}} + \dots)^2 \dots + \varepsilon^2 f_2(\lambda_a) \\ + \varepsilon^2 f_2'(\lambda_a)(\beta_1 \varepsilon^{\frac{1}{2}} + \beta_2 \varepsilon^{\frac{2}{2}} + \beta_3 \varepsilon^{\frac{3}{2}} + \dots) \\ + \varepsilon^2 \frac{f_2''(\lambda_a)}{2!} (\beta_1 \varepsilon^{\frac{1}{2}} + \beta_2 \varepsilon^{\frac{2}{2}} + \beta_3 \varepsilon^{\frac{3}{2}} + \dots)^2 \dots = 0 \quad (\text{A16})$$

The coefficients of the first-order term of ε on the left-hand side of (A16) should be equal to zero, i.e.,

$$f_0'(\lambda_a)\beta_2 + \frac{f_0''(\lambda_a)}{2!}\beta_1^2 + f_1(\lambda_a) = 0 \quad (\text{A17})$$

When $\lambda_a = \lambda_w$, from (A11),

$$f_0'(s)|_{s=\lambda_a} = 0, \quad f_0''(s)|_{s=\lambda_a} = 2 \quad (\text{A18})$$

From (A15), (A17) and (A18),

$$\Delta\lambda_a \approx \pm \beta_1 \varepsilon^{\frac{1}{2}} = \pm \sqrt{-\varepsilon f_1(\lambda_a)} = \pm \sqrt{-\varepsilon a_{2M-1}(\lambda_a)} \quad (\text{A19})$$

Similarly, it can be proved for λ_w that

$$\Delta\lambda_w \approx \pm \sqrt{-\varepsilon f_1(\lambda_w)} = \pm \sqrt{-\varepsilon a_{2M-1}(\lambda_w)} \quad (\text{A20})$$

According to the matrix theory [22], in (A8) and (A9) it should have

$$a_{2M-1}(s) = -\sum \text{diag}[\mathbf{h}(s)\mathbf{g}(s)] \quad (\text{A21})$$

From (A7) and (A21),

$$\varepsilon a_{2M-1}(s) = -(s - \lambda_a)(s - \lambda_w) \varepsilon \sum \text{diag}[\mathbf{H}(s)\mathbf{G}(s)] \quad (\text{A22})$$

From (A1) and (A22)

$$\varepsilon a_{2M-1}(s) = -(s - \lambda_a)(s - \lambda_w) \sum \text{diag}[\mathbf{W}(s)\mathbf{G}(s)] \quad (\text{A23})$$

Denote $G_{ji}(s)$ and $W_{ji}(s)$ as the j th-row and i th-column element of $\mathbf{G}(s)$ and $\mathbf{W}(s)$ respectively. Express $G_{ji}(s)$ and $W_{ji}(s)$ in the following form

$$\begin{aligned} G_{ji}(s) &= \frac{R_{aji}}{(s - \lambda_a)} + \sum_{k=1} \frac{R_{ajik}}{(s - \lambda_{ajik})} + d_{aji}, \\ W_{ji}(s) &= \frac{R_{wij}}{(s - \lambda_w)} + \sum_{k=1} \frac{R_{wijk}}{(s - \lambda_{wijk})} + d_{wij} \end{aligned} \quad (\text{A24})$$

From (A23) and (A24)

$$\begin{aligned} \varepsilon a_{2M-1}(s) &= -(s - \lambda_a)(s - \lambda_w) \left(\sum_{j=1} \left(\sum_{i=1} G_{ji}(s) W_{ij}(s) \right) \right) \\ &= - \left[\sum_{j=1} \left(\sum_{i=1} \left(R_{aji} + (s - \lambda_a) \left(\sum_{k=1} \frac{R_{ajik}}{(s - \lambda_{ajik})} + d_{aji} \right) \right) \right. \right. \\ &\quad \left. \left. \left(R_{wij} + (s - \lambda_w) \left(\sum_{k=1} \frac{R_{wijk}}{(s - \lambda_{wijk})} + d_{wij} \right) \right) \right) \right] \end{aligned} \quad (\text{A25})$$

Hence, when $\lambda_a = \lambda_w$, from (A25)

$$\varepsilon a_{2M-1}(\lambda_a) = \varepsilon a_{2M-1}(\lambda_w) = - \left(\sum_{j=1} \left(\sum_{i=1} R_{aji} R_{wij} \right) \right) \quad (\text{A26})$$

where R_{aji} and R_{wij} are the j th-row and i th-column elements of the residue matrices, \mathbf{R}_A and \mathbf{R}_W given in (8) and (9), respectively. Hence,

$$\varepsilon a_{2M-1}(\lambda_a) = \varepsilon a_{2M-1}(\lambda_w) = - \sum \text{diag}[\mathbf{R}_A \mathbf{R}_W] \quad (\text{A27})$$

From (A19), (A20) and (A27), (10) is proved.

REFERENCES

- [1] X. Xie, X. Zhang, H. Liu, C. Zhang, Y. Li, and H. Liu, "Characteristic analysis of subsynchronous resonance in practical wind farms connected to series-compensated transmissions," *IEEE Trans. Energy Convers.*, vol. 32, no. 3, pp. 1117–1126, Sep. 2017.
- [2] V. B. Virulkar and G. V. Gotmare, "Sub-synchronous resonance in series compensated wind farm: A review," *Renew. Sustain. Energy Rev.*, vol. 55, pp. 1010–1029, 2016.
- [3] H. A. Mohammadpour and E. Santi, "Sub-synchronous resonance analysis in DFIG-based wind farms: Definitions and problem identification — Part I," in *Proc. IEEE Energy Convers. Congr. Expo.*, 2014, pp. 812–819.
- [4] L. Wang, X. Xie, H. Liu, H. Li, Y. Li, and Q. Jiang, "Investigation of SSR in practical DFIG-based wind farms connected to a series-compensated power system," *IEEE Trans. Power Syst.*, vol. 30, no. 5, pp. 2772–2779, Sep. 2015.
- [5] G. Tang, Z. He, H. Pang, X. Huang and X. P. Zhang, "Basic topology and key devices of the five-terminal DC grid," *CSEE J. Power Energy Syst.*, vol. 1, no. 2, pp. 22–35, Jun. 2015.
- [6] L. Fan, R. Kavasseri, Z. L. Miao, and C. Zhu, "Modeling of DFIG-based wind farms for SSR analysis," *IEEE Trans. Power Del.*, vol. 25, no. 4, pp. 2073–2082, Oct. 2010.
- [7] W. Chen, X. Xie, H. Liu, H. Li, and D. Wang, "Probabilistic stability analysis of subsynchronous resonance for series-compensated DFIG-based wind farms," *IEEE Trans. Sustain. Energy*, vol. 9, no. 1, pp. 400–409, Jan. 2018.

- [8] W. Du, H. F. Wang, and R. Dunn, "Power system small-signal oscillation stability as affected by large-scale PV penetration," in *Proc. Int. Conf. Sustain. Power Gener. Supply*, Nanjing, China, 2009, pp. 1–6.
- [9] H. F. Wang and F. J. Swift, "A unified model for the analysis of FACTS devices in damping power system oscillations. I. Single-machine infinite-bus power systems," *IEEE Trans. Power Del.*, vol. 12, no. 2, pp. 941–946, Apr. 1997.
- [10] W. Du, X. Chen, and H. F. Wang, "A method of open-loop modal analysis to examine the SSOs in a multi-machine power system with multiple variable speed wind generators," *IEEE Trans. Power Syst.*, vol. 33, no. 4, pp. 4297–4307, Jul. 2017.
- [11] W. Du, Y. Wang, and H. F. Wang, "Concept of modal repulsion in examining the sub-synchronous oscillations in power system," *IEEE Trans. Power Syst.*, vol. 33, no. 4, pp. 4614–4624, Jul. 2018.
- [12] W. Du, C. Chen, and H. F. Wang, "Sub-synchronous oscillations induced by the DFIGs in power systems without series compensated lines," *IEEE Trans. Power Syst.*, vol. 9, no. 3, pp. 1275–1284, Jul. 2018.
- [13] P. Dattaray, D. Chakravorty, J. Yu, V. Terzija, and P. Wall, "A novel control strategy for subsynchronous resonance mitigation using 11 kV VFD-based auxiliary power plant loads," *IEEE Trans. Power Del.*, vol. 33, no. 2, pp. 728–740, Apr. 2018.
- [14] F. Zhang, L. Cheng, W. Gao, and R. Huang, "Synchrophasors-based identification for subsynchronous oscillations in power systems," *IEEE Trans. Smart Grid*, to be published, doi: [10.1109/TSG.2018.2792005](https://doi.org/10.1109/TSG.2018.2792005).
- [15] T. Rajaram, J. M. Reddy, and Y. Xu, "Kalman filter based detection and mitigation of subsynchronous resonance with SSSC," *IEEE Trans. Power Syst.*, vol. 32, no. 2, pp. 1400–1409, Mar. 2017.
- [16] M. A. Chowdhury and G. M. Shafiuallah, "SSR mitigation of series-compensated DFIG wind farms by a nonlinear damping controller using partial feedback linearization," *IEEE Trans. Power Syst.*, vol. 33, no. 3, pp. 2528–2538, May 2018.
- [17] M. A. Chowdhury, M. A. Mahmud, H. R. Pota, and W. Shen, "Nonlinear controller design for series-compensated DFIG-based wind farms to mitigate subsynchronous control interaction," *IEEE Trans. Energy Convers.*, vol. 32, no. 2, pp. 707–719, Jun. 2017.
- [18] P. Kundur, *Power System Stability and Control*. New York, NY, USA: McGraw-Hill, 1994.
- [19] IEEE subsynchronous resonance task force, "First benchmark model for computer simulation of subsynchronous resonance," *IEEE Trans. Power Syst.*, vol. PWRS-96, no. 5, pp. 1565–1572, Sep. 1977.
- [20] S. Li, T. A. Haskew, R. P. Swatloski, and W. Gathings, "Optimal and direct-current vector control of direct-driven PMSG wind turbines," *IEEE Trans. Power Electron.*, vol. 27, no. 5, pp. 2325–2337, May 2012.
- [21] M. I. Višik and L. A. Ljusternik, "The solution of some perturbation problems in the case of matrices and self-adjoint and non-self-adjoint differential equations," *Russian Math. Surveys*, vol. 15, no. 3, pp. 1–73, 2007.
- [22] J. H. Wilkinson, *The Algebraic Eigenvalue Problem*. Oxford, U.K.: Clarendon, 1965.



Wenjuan Du (M'14) received the Ph.D. degree from the University of Bath, Bath, U.K., in 2009. She is currently a Full Professor with the School of Electrical and Electronic Engineering, North China Electric Power University, Beijing, China. Her main research interests include power system stability analysis and control, including energy storage systems, FACTS, EV, and renewable power generations.

Qiang Fu is working toward the Ph.D. degree with the School of Electrical and Electronic Engineering, North China Electric Power University, Beijing, China. His main research interests include power system stability analysis and control considering wind power integration.

Haifeng Wang (M'96–SM'02) is a Full Professor with the School of Electrical and Electronic Engineering, North China Electric Power University, Beijing, China. He had worked in the U.K. for years and was the Chair in Electrical Engineering and a Full Professor with the Queen's University Belfast, Belfast, U.K., before he moved to Beijing. His main research interest focuses on power system stability analysis and control.